Photo-molecular high temperature superconductivity

M. Buzzi[1,*], D. Nicoletti[1], M. Fechner[1], N. Tancogne-Dejean[1], M. A. Sentef[1], A. Georges[2,3], T. Biesner[4], E. Uykur[4], M. Dressel[4], A. Henderson[5], T. Siegrist[5], J. A. Schlueter[5,6], K. Miyagawa[7], K. Kanoda[7], M.-S. Nam[8], A. Ardavan[8], J. Coulthard[8], J. Tindall[8], F. Schlawin[8], D. Jaksch[8], A. Cavalleri[1,8,*]

[1] *Max Planck Institute for the Structure and Dynamics of Matter, 22761 Hamburg, Germany*

[2] *Center for Computational Quantum Physics (CCQ), The Flatiron Institute, New York, NY 10010, USA*

[3] *Collège de France, 11 place Marcelin Berthelot, 75005 Paris, France*

[4] *1. Physikalisches Institut, Universität Stuttgart, 70569 Stuttgart, Germany*

[5] *National High Magnetic Field Laboratory, 1800 E Paul Dirac Drive, Tallahassee, FL 31310, USA*

[6] *Division of Material Research, National Science Foundation, Alexandria, VA 22314, USA*

[7] *Department of Applied Physics, University of Tokyo, 7-3-1 Hongo, Bunkyo-ku, Tokyo 113-8656, Japan*

[8] *Department of Physics, Clarendon Laboratory, University of Oxford, Oxford OX1 3PU, United Kingdom*

** e-mail: michele.buzzi@mpsd.mpg.de, andrea.cavalleri@mpsd.mpg.de*

Supplementary Material

S1. Sample preparation and equilibrium optical properties

Single crystals of κ-(BEDT-TTF)$_2$Cu[N(CN)$_2$]Br with typical dimensions of $0.5 \times 0.3 \times 0.5\ \mathrm{mm}^3$ were synthesized by electro-crystallization, following the procedure described in Refs. 1 & 2. The (ac)-axes define the highly conducting plane, while the b-axis is normal to that plane. The equilibrium superconducting transition at $T_C \simeq 12.5$ K was characterized with resistivity measurements[1,2].

The terminal ethylene groups of the BEDT-TTF molecule (henceforth abbreviated ET) in this compound undergo an ordering transition, at about 80 K. To ensure minimum disorder of the ethylene groups, in all of our experiments the samples were cooled down at the same low rate of ~150 mK/min below 160 K[1,2].

The κ-(ET)$_2$Cu[N(CN)$_2$]Br equilibrium optical properties were measured using a Bruker Vertex 80v interferometer. The sample was mounted on the tip of a cone-shaped holder, with the in-plane crystal surface exposed to the beam. The holder was installed on the cold finger of a He-flow cryostat, thus enabling to collect broadband infrared spectra in reflection geometry at different temperatures. These spectra were then referenced against a thin gold film evaporated in-situ on the same sample surface.

The reflectivity curves obtained with this procedure, covering a range between ~25 – 5000 cm^{-1}, were extrapolated to $\omega \to 0$ with Drude fits (see also Section S3), and extended to higher frequencies with literature data[3,4]. This allowed us to perform Kramers-Kronig transformations and retrieve full sets of in-plane equilibrium response functions to be used as reference in our pump-probe experiment.

Examples of selected reflectivity and complex optical conductivity spectra are reported in Fig. S1. As discussed in the main text, the normal state equilibrium response is characterized by a metallic Drude peak (see Fig. S1b) for temperatures below $T^* \simeq 50$ K, while the spectra at higher temperatures are those of a "bad metal", characterized by a non-zero low-frequency conductivity, in absence of a Drude peak (see also Ref. 3).

We did not observe any change in the optical spectra across the superconducting transition temperature $T_C = 12.5$ K. The absence of a clear optical gap in the superconducting κ-(ET)$_2$X compounds has already been reported in the past[5-8].

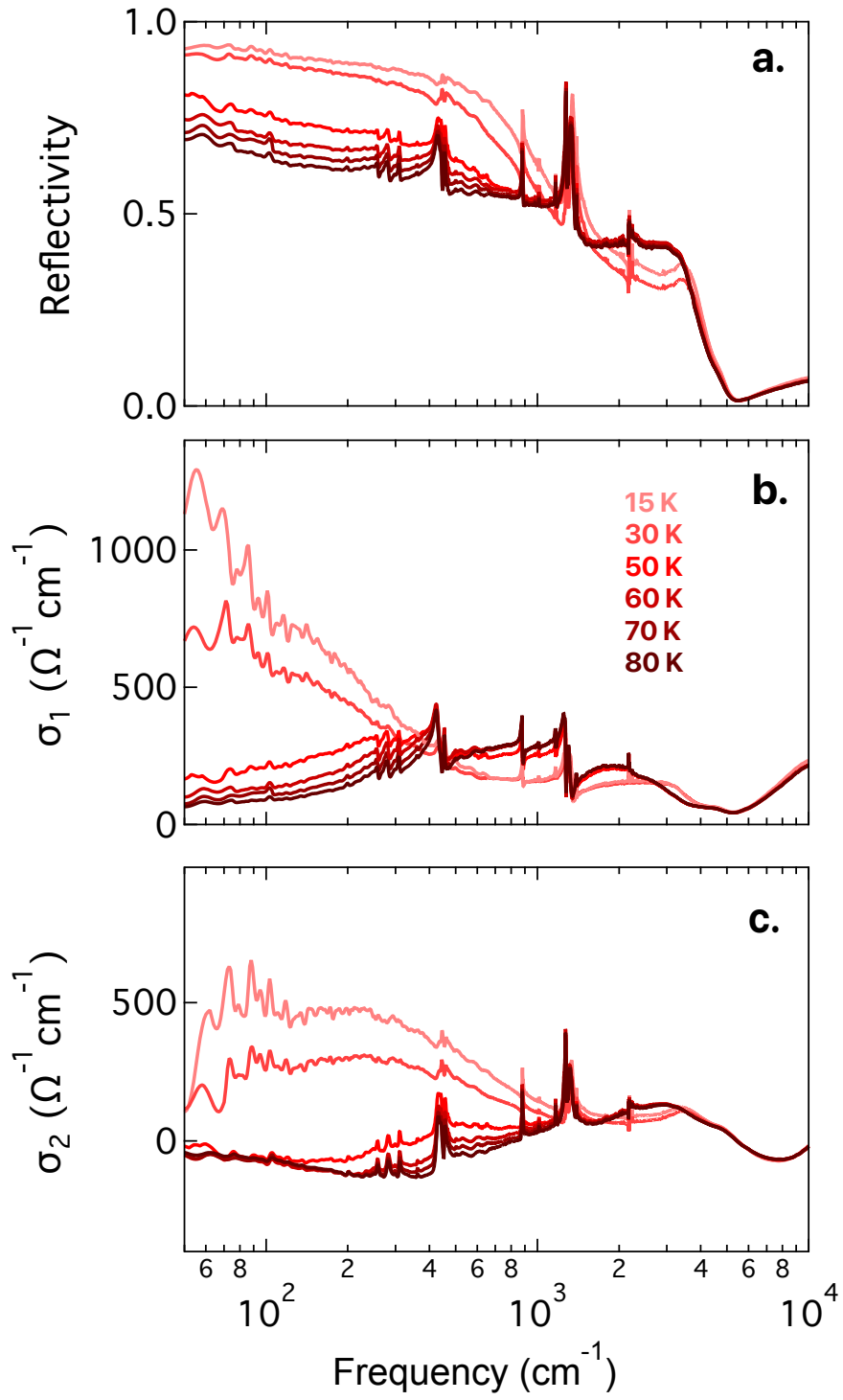

Fig. S1. Equilibrium in-plane reflectivity (a), real (b), and imaginary part (c) of the optical conductivity of κ-$(ET)_2Cu[N(CN)_2]Br$, measured at different temperatures following the procedure described in the text.

S2. Determination of the transient optical properties

In a series of mid-infrared pump / THz probe experiments, we investigated different κ-$(ET)_2Cu[N(CN)_2]Br$ single crystals. Each of them was glued on the top of a cone-shaped sample holder, exposing a crystal face which contained both an in-plane and an out-of-plane axis (with ∼0.5 mm and ∼0.3 mm dimension, respectively). The holder was installed on the cold finger of a He-flow cryostat for temperature dependent measurements.

κ-$(ET)_2Cu[N(CN)_2]Br$ was photo-excited with ∼100 fs long mid-infrared pulses, tuned to different wavelengths ($\lambda_{pump} \simeq$ 11 μm, 8 μm, 6.8 μm, 5 μm), some of which were resonant with local vibrational modes of the ET molecules. These pump pulses were generated by difference frequency mixing of the signal and idler outputs of an optical parametric amplifier (OPA) in a 0.5 mm thick GaSe crystal. The OPA was pumped with ∼100 fs long pulses from a commercial Ti:Sapphire regenerative amplifier (800-nm wavelength).

The pump pulses were focused onto the sample surface, with their polarization aligned along the out-of-plane axis. The typical pump spot size was ∼0.5 mm, allowing for a full illumination of the crystal surface. A maximum fluence of ∼4 mJ/cm^2 could be achieved, corresponding to a peak electric field of ∼4 MV/cm.

The transient reflectivity changes after photo-excitation were determined via time-domain THz spectroscopy in two different experimental setups. Single-cycle THz pulses were generated either in 1-mm thick ZnTe or in 0.2-mm thick GaP, using 100-fs and 30-fs long 800 nm pulses, respectively. These probe pulses were focused at normal incidence onto the sample surface on a spot of ≲ 0.3 mm diameter. Their polarization was set along the in-plane direction, and their electric field profile was measured, after reflection, via electro-optic sampling in nonlinear crystals identical to those used for THz generation (*i.e.*, 1-mm thick ZnTe and 0.2-mm thick GaP). The ZnTe based setup produced a spectral bandwidth extending from ∼25 to 70 cm^{-1}, while the GaP based setup covered the range from ∼40 to 230 cm^{-1}.

In order to minimize the effects on the pump-probe time resolution due to the finite duration of the THz probe pulse, we performed the experiment as described in Ref. 9. The transient reflected field at each time delay τ after excitation was obtained by

keeping fixed the delay τ between the pump pulse and the electro-optic sampling gate pulse, while scanning the delay t of the single-cycle THz probe pulse.

The stationary probe electric field $E_R(t)$ and the differential electric field $\Delta E_R(t,\tau)$ reflected from the sample were recorded simultaneously by feeding the electro-optic sampling signal into two lock-in amplifiers and mechanically chopping the pump and probe beams at different frequencies. $E_R(t)$ and $\Delta E_R(t,\tau)$ were then independently Fourier transformed to obtain the complex-valued, frequency-dependent $\tilde{E}_R(\omega)$ and $\Delta\tilde{E}_R(\omega,\tau)$. The photo-excited complex reflection coefficient $\tilde{r}(\omega,\tau)$ was determined by

$$\frac{\Delta\tilde{E}_R(\omega,\tau)}{\tilde{E}_R(\omega)} = \frac{\tilde{r}(\omega,\tau) - \tilde{r}_0(\omega)}{\tilde{r}_0(\omega)},$$

where $\tilde{r}_0(\omega)$ is the stationary reflection coefficient known from the equilibrium optical response (see Section S1).

As the penetration depth of the excitation pulses was typically larger than that of the THz probe pulses (with the only exception of the 6.8 μm pump experiment, see Figure S2), the THz probe pulse sampled a homogeneously excited volume. The transient optical properties could then be extracted directly, without the need to consider any pump-probe penetration depth mismatch in the data analysis.

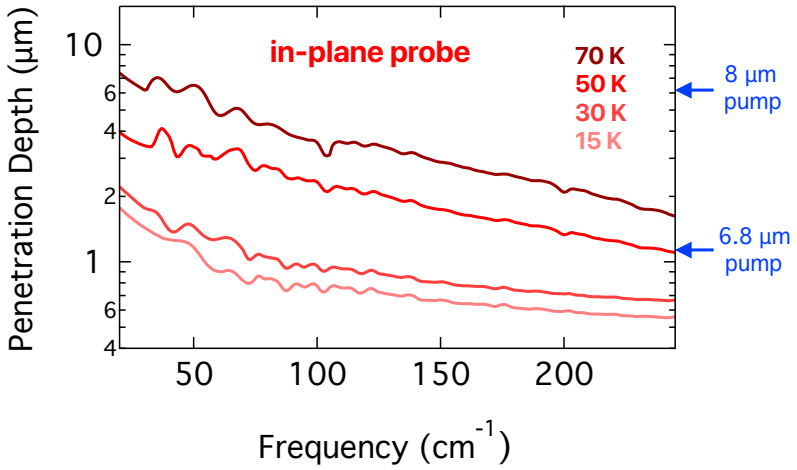

Fig. S2. Field penetration depth, $d(\omega) = \frac{c}{\omega \cdot \mathrm{Im}[\tilde{n}_0(\omega)]}$ (here $\tilde{n}_0(\omega)$ is the stationary complex refractive index), calculated from the in-plane equilibrium optical properties of κ-$(ET)_2Cu[N(CN)_2]Br$ (see Fig. S1), at selected temperatures. Data are displayed over the frequency range covered by our THz probe pulses. Arrows on the right axis indicate the corresponding out-of-plane pump penetration depth values for two selected excitation frequencies, extracted from the data in Ref. 10.

In this case, the complex refractive index of the photo-excited material, $\tilde{n}(\omega,\tau)$, was directly retrieved from the Fresnel relation:

$$\tilde{n}(\omega,\tau) = \frac{\tilde{\mathrm{r}}(\omega,\tau) - 1}{\tilde{\mathrm{r}}(\omega,\tau) + 1},$$

and from this, the transient complex optical conductivity, $\tilde{\sigma}(\omega,\tau) = \frac{\omega}{4\pi i}[\tilde{n}(\omega,\tau)^2 - \varepsilon_\infty]$.

For the limited set of data that required a pump-probe penetration depth analysis ($\lambda_{pump} = 6.8$ µm, $T \geq 50$ K), we followed the procedure described in Refs. 11 & 12. We treated the photo-excited surface as a stack of thin layers with a homogeneous refractive index and described the excitation profile by an exponential decay. By numerically solving the coupled Fresnel equations of such multi-layer system, the refractive index at the surface could be retrieved, and from this the complex conductivity for a homogeneously transformed volume.

Importantly, this renormalization only affected the size of the response, whereas the qualitative changes in optical properties were independent of it and the specific model chosen[12].

S3. Data analysis and fitting models

The in-plane equilibrium optical properties of κ-$(ET)_2Cu[N(CN)_2]Br$ were fitted at all measured $T > T_C$ with a Drude-Lorentz model, for which the complex optical conductivity is expressed as:

$$\tilde{\sigma}_{DL}(\omega) = \frac{\omega_p^2}{4\pi}\frac{1}{\gamma_D - i\omega} + \sum_i \frac{\Omega_{p,i}^2}{4\pi}\frac{\omega}{i\left(\Omega_{0,i}^2 - \omega^2\right) + \Gamma_i\omega}. \quad \text{(S3.1)}$$

Here, ω_p and γ_D are the Drude plasma frequency and momentum relaxation rate, while $\Omega_{0,i}$, $\Omega_{p,i}$, and Γ_i are the peak frequency, plasma frequency, and damping coefficient of the i-th oscillator, respectively.

The same Drude-Lorentz model was also employed to fit the transient optical spectra after photo-excitation. Here, all parameters related to the oscillators at frequencies outside the measurement range were kept fixed to the values determined at equilibrium, while the lowest frequency oscillator and the Drude term were left free to vary. Importantly, for each data set, the same parameters were used to simultaneously fit the reflectivity, the real part of the optical conductivity, as well as its imaginary part. As shown, for example, in Fig. 3 & Fig. 6 of the main text, this Drude-Lorentz model is able to fully reproduce the experimental data for the temperatures and time delays that show a metallic behavior and no signature of a superconducting-like response.

In addition, the transient superconducting-like response of κ-$(ET)_2Cu[N(CN)_2]Br$ could also be captured (see fits in Fig. 6 of main text) by the simple $\gamma_D \to 0$ limit of Eq. S3.1,

$$\tilde{\sigma}_{DL}(\omega, \gamma_D \to 0) = \frac{\pi}{2}\frac{N_S e^2}{m}\delta[\omega = 0] + i\frac{N_S e^2}{m}\frac{1}{\omega} + \sum_i \frac{\Omega_{p,i}^2}{4\pi}\frac{\omega}{i\left(\Omega_{0,i}^2 - \omega^2\right) + \Gamma_i\omega}. \quad \text{(S3.2)}$$

Here N_S, e, and m are the superfluid density, electron charge, and electron mass, respectively.

That said, the Drude-Lorentz model of Eq. S3.1 could be applied to all transient optical spectra reported in this work, without any assumption on the nature of the non-equilibrium state (see also Ref. 13). The zero-frequency limit $\sigma_0 = \lim_{\omega\to 0} \tilde{\sigma}_{DL}(\omega)$ extracted from these fits (see Fig. 5 & Fig. 6 of main text), which is a finite quantity in a

metal and diverges in a "perfect conductor", was used as a discriminator for the presence of transient superconductivity[13].

Additional fitting of the superconducting-like optical properties was performed with an extension of the Mattis-Bardeen model for superconductors of variable purity[14,15], which is typically used to describe the response of superconductors at equilibrium, for finite frequencies and temperatures. Fit curves extracted with this procedure are reported, for example, in Fig. 3 of the main text. The corresponding values of the optical gap, $2\Delta(T)$, are shown in Fig. 4a.

In addition, in Figures 4b & 5b we display the temperature and time-delay dependence of the transient superfluid density. This quantity can either be determined from the low-frequency divergence in the imaginary conductivity, as $N_{eff}^{Trans} = \frac{mV_{Cell}}{e^2} \lim_{\omega \to 0}[\omega \sigma_2^{Trans}(\omega)]$ or, alternatively, via the integrated spectral weight loss over the optical gap, as $N_{eff}^{Trans} \propto \int \left[\sigma_1^{Equil}(\omega) - \sigma_1^{Trans}(\omega)\right] d\omega$ (see Fig. 5a of main text).

We used this latter expression to estimate the experimental uncertainty on N_{eff}^{Trans}. Its value depends, in fact, on how $\sigma_1^{Trans}(\omega)$ is extrapolated below the measured spectral range ($\omega \lesssim 40$ cm^{-1}). Two cases can be considered: one where $\sigma_1^{Trans}(\omega)$ is completely gapped down to $\omega = 0$, and another one in which no spectral weight is lost below $\omega \simeq 40$ cm^{-1} (i.e., $\sigma_1^{Trans}(\omega < 40\ \text{cm}^{-1}) = \sigma_1^{Equil}(\omega < 40\ \text{cm}^{-1})$). If we extract these values at the peak of the pump-probe response in Fig. 5a ($\sim$1 ps time delay), we obtain in the former case $\sim 1.12 \cdot 10^5\ \Omega^{-1}\text{cm}^{-2}$ and in the latter $\sim 0.91 \cdot 10^5\ \Omega^{-1}\text{cm}^{-2}$. This corresponds to a $\sim$20% uncertainty in the transient superfluid density.

Regardless of the above, we stress here that our analysis and interpretation does not rely on the absolute value of this quantity. Rather, we consider how it evolves with decreasing temperature vis-à-vis the equilibrium concentration of normal carriers and discover that both follow the same temperature dependence.

S4. Extended data sets

We report here a comparison of transient optical spectra taken under the same conditions (temperature, excitation wavelength and fluence, pump-probe time delay) on three different κ-$(ET)_2Cu[N(CN)_2]Br$ crystals coming from the same batch of samples.

These data, measured at $T = 30$ K, are reported in Fig. S4. Therein, we show how, aside from small differences, the non-equilibrium response appears to be sample independent, and all signatures of transient, photo-induced superconductivity, i.e., a reflectivity equal to 1, a gap in $\sigma_1(\omega)$, and a $\sim 1/\omega$ divergence in $\sigma_2(\omega)$, are fully preserved.

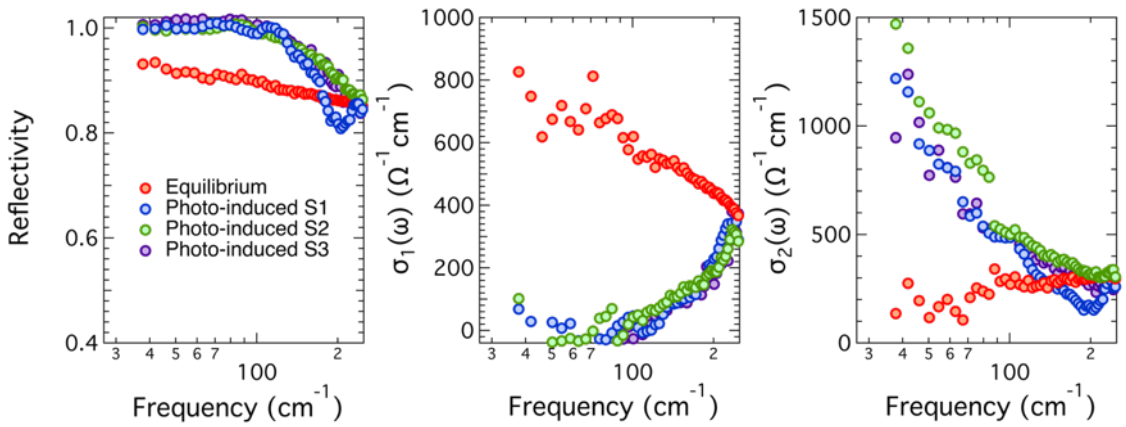

Fig. S4. In-plane reflectivity, real, and imaginary part of the optical conductivity, measured at $T = 30$ K under the very same excitation conditions ($\upsilon_{pump} = 1250$ cm^{-1}, ~2 mJ/cm^2 fluence) on three different κ-$(ET)_2Cu[N(CN)_2]Br$ crystals, at $\tau = 1$ ps pump-probe time delay (blue, green, and purple circles). Red data points are the spectra measured at equilibrium.

S5. Pump fluence dependence

In Figure S5 we show pump fluence dependent data. In analogy with Fig. 4 of the main text, we plot the non-equilibrium "superfluid density", determined from the low-frequency extrapolation of the transient imaginary conductivity as $N_{eff}^{Trans} = \frac{mV_{Cell}}{e^2} \lim_{\omega \to 0}[\omega \sigma_2^{Trans}(\omega)]$, where m is the bare electron mass, V_{Cell} the unit cell volume, and e the electron charge. This effective number of "condensed" carriers displays a monotonic increase with increasing excitation strength, with signatures of a saturation for fluences above ~2 mJ/cm^2.

The saturation seems to occur for a value of N_{eff}^{Trans} that approaches the equilibrium quasi-particle density, $N_{eff}^{Equil} = \frac{mV_{Cell}}{4\pi e^2}\left(\omega_P^{Equil}\right)^2$, which we show for reference as a horizontal dashed line (here ω_P^{Equil} is the equilibrium carrier plasma frequency extracted from Drude-Lorentz fits).

This observation, combined with the temperature dependent data of Fig. 4b of the main text, is suggestive of an intimate connection between the photo-excited carriers in the transient superconducting state and pre-existing quasiparticles at equilibrium.

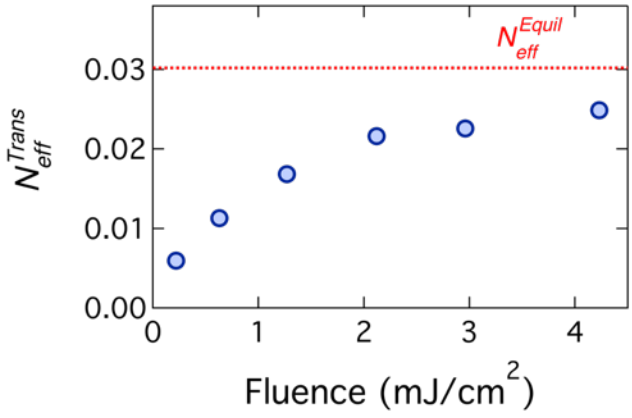

Fig. S5. Pump fluence dependence of the effective number of "condensed" carriers per unit cell in the transient state, N_{eff}^{Trans} (blue circles), shown along with the effective number of mobile carriers in the equilibrium metallic state before photo-excitation, N_{eff}^{Equil} (horizontal dashed line, see discussion in the text). These data have been taken upon 1250 cm^{-1} excitation at T = 50 K.

S6. Calculation of the effective Hubbard parameters

Geometry optimization

We performed a geometry optimization of the crystal structure for κ-Br in order to obtain relaxed atomic coordinates. This was achieved using the density functional theory code Quantum ESPRESSO[16,17] starting from the x-ray crystallographic data of Ref. 18. We used the PBE functional complemented by the Grimm D2 van der Waals correction, norm-conserving pseudopotentials, a $2 \times 1 \times 3$ momentum grid, an energy cutoff of 1224 eV, and a finite-temperature smearing of 10 meV. Forces were optimized to be smaller than 10^{-4} Ha/Bohr. We obtained relaxed lattice constants of 12.816 Å, 29.608 Å, and 8.493 Å, for the *a*, *b*, and *c* crystallographic directions, respectively. These values are in excellent agreement with reported measured values[18,19].

Phonon mode calculations

We computed the phonon modes of the isolated ET dimer and constructed the B_u modes by applying the corresponding symmetries[20]. These B_u modes are the infrared-active modes with dipole along the out-of-plane *b* direction. We obtained the eigenvectors of the dynamical matrix from Quantum ESPRESSO, using the same parameters and cell as for the geometry optimization of the full κ-Br crystal.

Figure S6.1 shows examples of eigenvectors for two modes with frequencies close to the experimental excitation conditions. While the 10.7 μm vibration (terminal ethylene mode) involves motions of the ethylene groups at the ends of each ET molecule, the 6.8 μm mode (C=C stretching mode) acts almost exclusively on the C atoms.

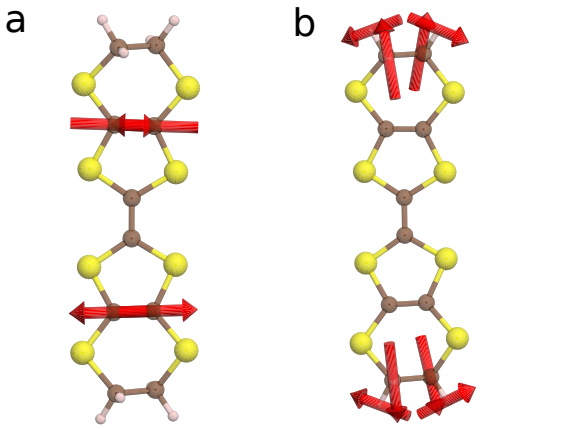

Fig. S6.1. Calculated B_u phonon mode eigenvectors corresponding to excitation wavelengths considered in this work. Here, the modes are displayed only for a single ET molecule.

Extraction of ground-state Hubbard model parameters

The effective electronic parameters of the weak-bond triangular lattice Hubbard model were obtained following the approach proposed in Ref. 21. To this end we computed the ground state and corresponding band structure using the Octopus code[22,23]. We employed the same norm-conserving pseudopotentials, PBE functional, and k-point grid as for the geometry optimization. The real-space grid was sampled with a spacing of 0.3 Bohr. The resulting band structure (Fig. S6.2) was fitted by a tight-binding model for 8 ET sites, leading to four parameters ($t_1 - t_4$), and fixing the electronic occupation to 3/4 filling[24]. From these fits, we extracted the effective parameters U, t, and t' of the single band Hubbard model[21,24] involving only the electronic band that crosses the Fermi level in Fig. S6.2.

$$H = \sum_{<ij>,\sigma} t\left(c_{i\sigma}^{\dagger} c_{j\sigma} + H.c.\right) + \sum_{[ij],\sigma} t'\left(c_{i\sigma}^{\dagger} c_{j\sigma} + H.c.\right) + U \sum_{i} \left(n_{i\uparrow} - \frac{1}{2}\right)\left(n_{i\downarrow} - \frac{1}{2}\right)$$

Note that the single-band Hubbard model is half-filled for the ¾-filled two-band tight-binding model.

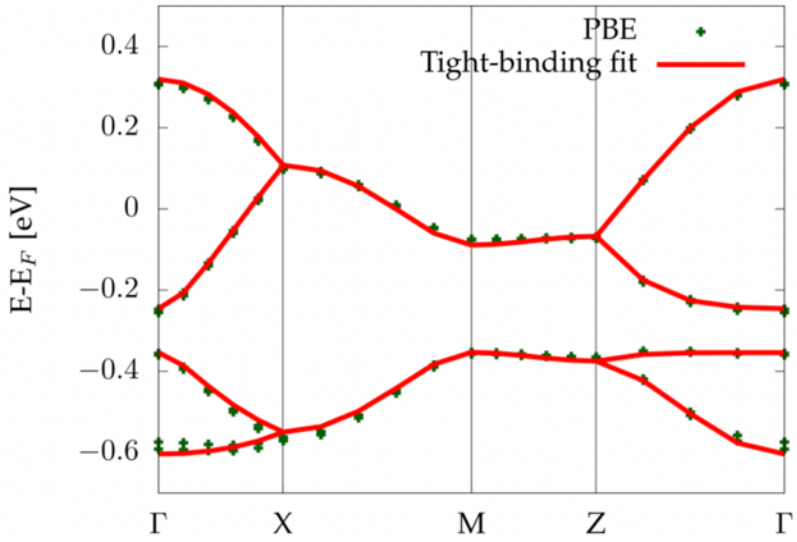

Fig. S6.2. Ground-state band structure of κ-Br calculated at the PBE level and tight-binding fit.

For κ-Br, the Cu 3d bands overlap with the ET molecule bands, complicating the extraction of the tight-binding parameters, as noted in Ref. 21,25. As DFT with semi-local functionals suffers from the so-called delocalization problem, and 3d transition metal bands are not well-described, we included a Hubbard U of 7 eV on the Cu 3d orbitals, which has the effect of improving the description of the electronic structure and it also shifts down the Cu 3d bands, thus making the fitting procedure more robust. For the equilibrium, undistorted structure, we obtained values of $U/t = 4.73$ and $t'/t = 0.24$. The U/t value is comparable to that reported in Ref. 21, but t'/t comes out smaller. This deviation is attributed to our inclusion of the van der Waals corrections for the geometry relaxation, which were not considered in Ref. 21. The van der Waals corrections significantly affect the volume of the relaxed crystal.

Extraction of Hubbard model parameters for displaced structures

Starting from the geometrically relaxed structure, we systematically displaced the ions according to the phonon mode coordinates obtained in the calculations. For each displaced structure, we computed the adiabatic electronic ground state and band structure in the frozen-phonon approximation using the Octopus code with the same technical parameters employed in the ground state calculation. We then followed exactly the same steps as in the ground state case to perform the tight-binding fits and

finally extracted the effective Hubbard model parameters. Figure S6.3 shows the resulting modulations of U, t, and the ratios U/t and t'/t for displacements along the B_u mode coordinates.

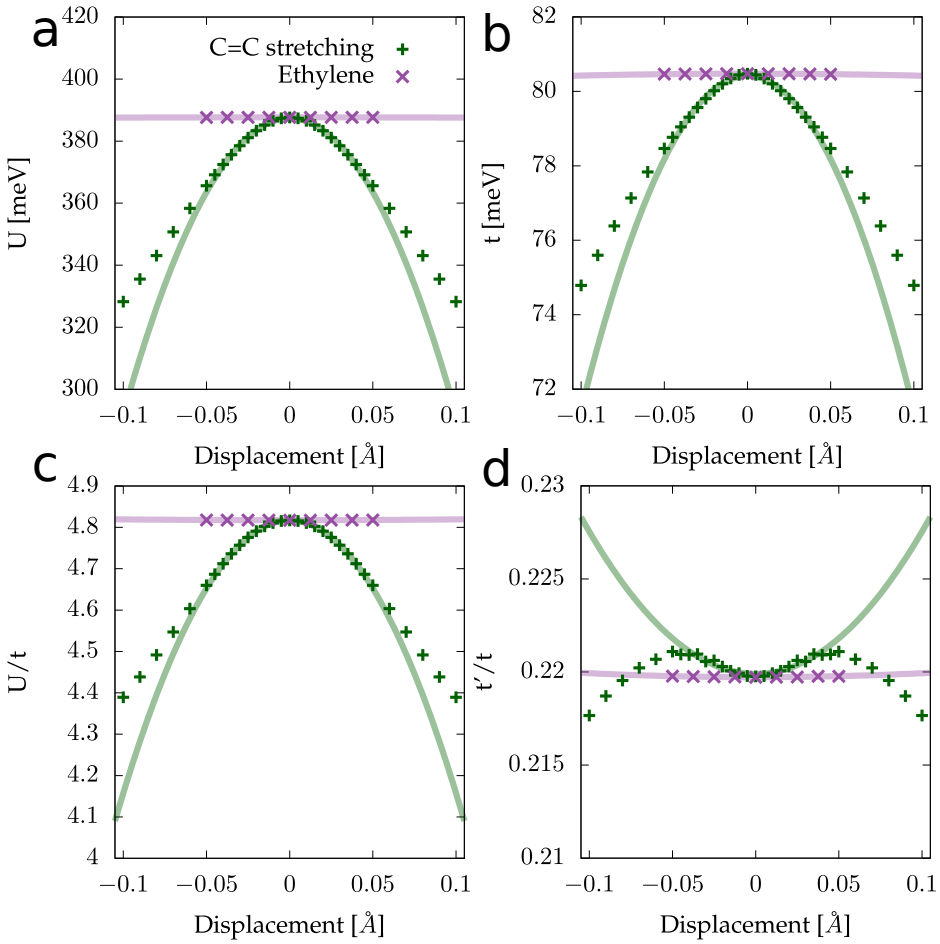

Fig. S6.3. Hubbard model parameters as a function of mode displacement. **(a)** On-dimer Hubbard interaction U, **(b)** strong bond hopping integral, t, **(c)** ratio U/t, and **(d)** t'/t. In each plot the lines represent parabolic fits to the data. Structural deformations along the normal coordinates of the C=C stretch induce strong, non-linear modifications of the electronic interaction parameters (green lines and symbols). By contrast, displacement of the terminal ethylene mode does not induce significant changes (purple lines and symbols).

S7. Driven Hubbard model

The geometry of the triangular Fermi-Hubbard model considered here is shown in Fig. S7.1. The driven Hamiltonian is given by:

$$H(\tau) = \sum_{<ij>,\sigma} t(\tau)\left(c_{i\sigma}^{\dagger}c_{j\sigma} + H.c.\right) + \sum_{[ij],\sigma} t'\left(c_{i\sigma}^{\dagger}c_{j\sigma} + H.c.\right) + U(\tau)\sum_{i}\left(n_{i\uparrow} - \frac{1}{2}\right)\left(n_{i\downarrow} - \frac{1}{2}\right), \quad (S7.1)$$

where τ denotes the time, t is the nearest neighbout hopping element and t' is the hopping element in the vertical direction. Following the frozen phonon simulations reported in Section S6, we assumed the on-site interaction U and the strong bond hopping elements t to be modulated by the phonon driving as follows:

$$U(\tau) = U_0 * \left(1 - A_1 \sin^2(\Omega\tau) e^{-\frac{(\tau-\tau_0)^2}{(2\tau_w)^2}}\right),$$

$$t(\tau) = t_0 * \left(1 - A_2 \sin^2(\Omega\tau) e^{-\frac{(\tau-\tau_0)^2}{(2\tau_w)^2}}\right). \quad (S7.2)$$

Here, the amplitudes A_1 and A_2 were extracted from the calculations in Section S6, the modulation frequency Ω was set to the phonon frequency, while the parameters τ_w and τ_0 control the duration and delay of the sinusoidal pulse. We assumed that the vertical hopping strength t' remains constant.

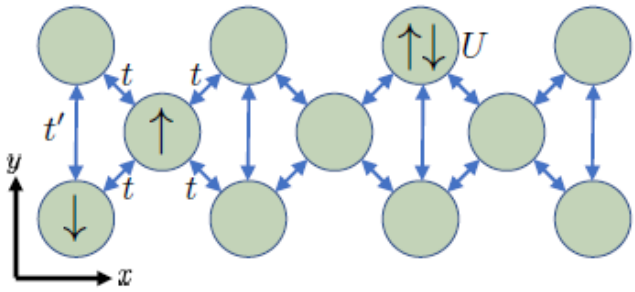

Fig. S7.1. A sketch of the geometry of the Hubbard ladder investigated in our study. Electrons can hop between nearest neighbour sites with amplitude t, and vertically with amplitude t'. Two electrons occupying the same site experience a repulsion U.

In Fig. S7.2 we report surface plots of the doublon correlations in distance and time for various system sizes. For sufficiently large systems we observe the emergence of uniform long-range doublon correlations which stabilise and persist over the simulation timescale. The increase in long-range correlation strength becomes more pronounced as the system size increases.

Finally, in Fig. S7.3 we show the full time-dynamics of the doublon correlations for various driving strengths and a fixed system size.

The matrix product calculations used to produce these results were performed using the Tensor Network Library[26]. The system was initialised in its ground state using the Density Matrix Renormalisation Group algorithm[27] whilst the time evolution was performed with the Time Evolving Block Decimation method[28] on the resulting initial state. We used a second order Suzuki-Trotter decomposition of the time evolution operator with a time-step of $\delta\tau t = \pi\Omega/50$. In all our calculations we ensured that our results remained unchanged upon increasing the bond dimension from the specified value in the figures.

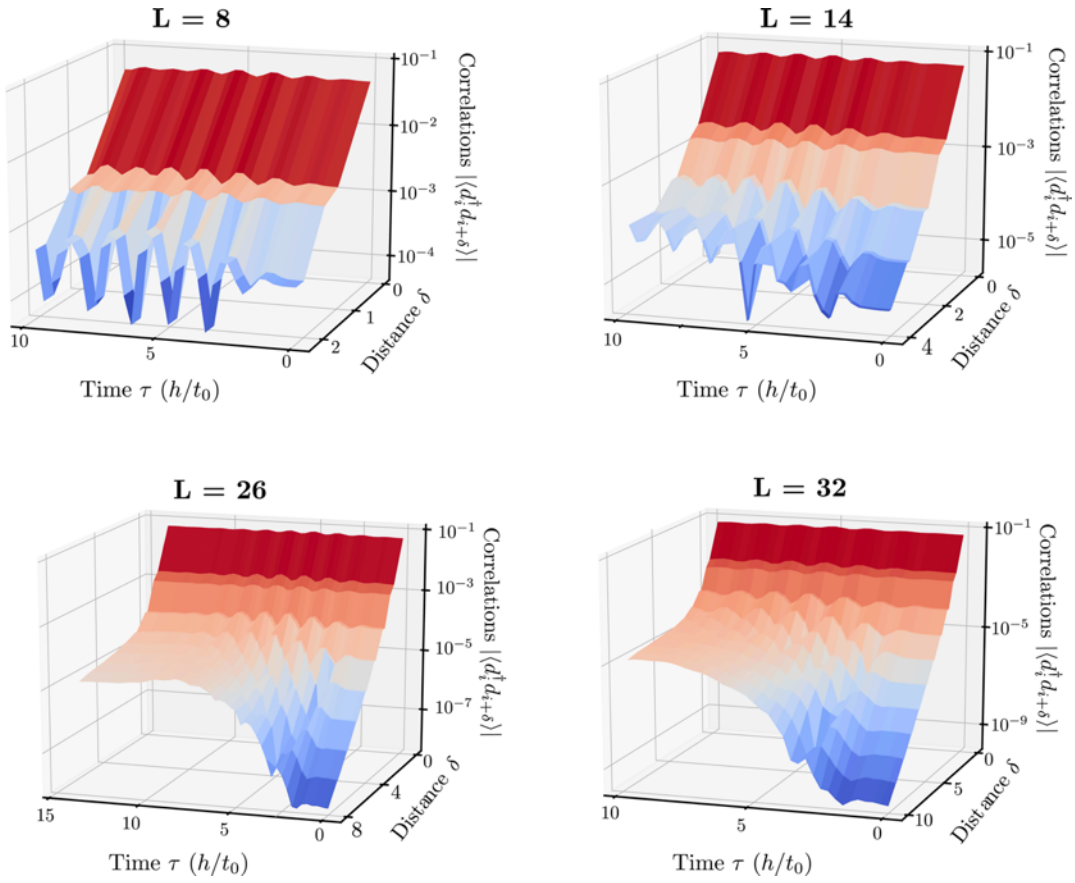

Fig. S7.2. Doublon Correlations as a function of distance (in lattice units) and time (in units of h/t_0) for the triangular ladder Hubbard model described by the Hamiltonian in Eq. (1). The four panels show calculations for four different system sizes L. The system is initialised in its ground state with $U_0 = 4.82\, t_0, t' = 0.22 t_0$ and half-filling. It was then allowed to evolve under time-modulated interaction strengths (see Eq. S7.2) with driving parameters $\tau_0 = 5.0 t_0$, $\tau_w = 5.0 t_0$, $\Omega = 2.27 t_0$, $A_1 = 0.155$ and $A_2 = 0.07$.

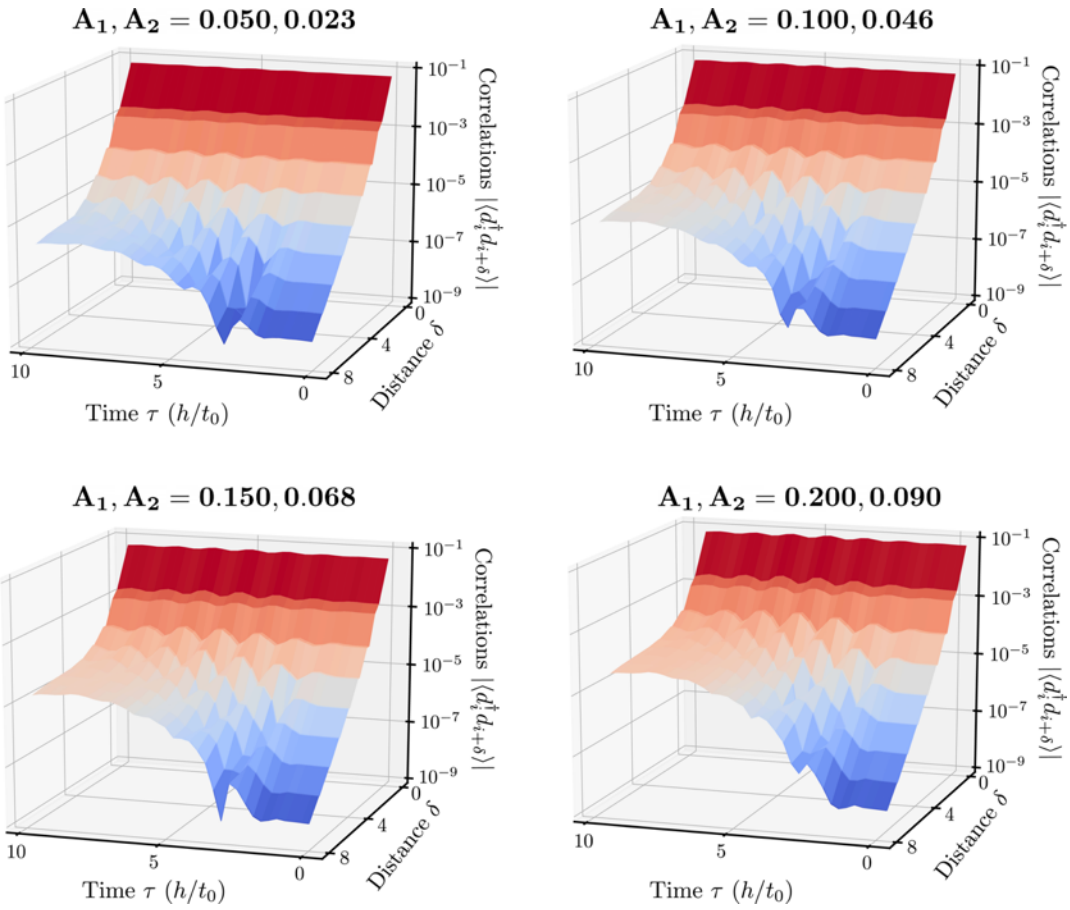

Fig. S7.3. Doublon correlations as a function of distance (in lattice units) and time (in units of h/t_0) for the 26-site triangular ladder Hubbard model described by the Hamiltonian in Eq. S7.1. The four panels show calculations for different driving amplitudes A_1, A_2. The system was initialised in its ground state with $U_0 = 4.73t_0, t' = 0.24t_0$, at half filling. It was then allowed to evolve under time-modulated interaction strengths (see Eq. S7.2) with driving parameters $\tau_0 = 5.0t_0$, $\tau_w = 5.0t_0$, $\Omega = 2.27t_0$, and constant ratio $A_1/A_2 = 2.21$.

References (Supplementary Material)

1 Nam, M.-S., Ardavan, A., Blundell, S. J. & Schlueter, J. A. Fluctuating superconductivity in organic molecular metals close to the Mott transition. *Nature* **449**, 584, (2007).

2 Nam, M.-S. *et al.* Superconducting fluctuations in organic molecular metals enhanced by Mott criticality. *Scientific Reports* **3**, 3390, (2013).

3 Eldridge, J. E. *et al.* Infrared optical properties of the 12K organic superconductor κ-(BEDT-TTF)$_2$Cu[N(CN)$_2$]Br. *Solid State Communications* **79**, 583-589, (1991).

4 Faltermeier, D. *et al.* Bandwidth-controlled Mott transition in κ-(BEDT-TTF)$_2$Cu[N(CN)$_2$]Br$_x$Cl$_{1-x}$: Optical studies of localized charge excitations. *Physical Review B* **76**, 165113, (2007).

5 Kornelsen, K. E., Eldridge, J. E., Wang, H. H. & Williams, J. M. Far-infrared optical absorption of the 10.4 K organic superconductor κ-(BEDT-TTF)$_2$[Cu(NCS)$_2$]. *Solid State Communications* **76**, 1009-1013, (1990).

6 Kornelsen, K. E. *Infrared Optical Properties of the Organic Superconductor κ-(BEDT-TTF)$_2$[Cu(NCS)$_2$]*, University of British Columbia, (1990).

7 Ichimura, K., Suzuki, K., Nomura, K. & Kawamoto, A. Tunneling spectroscopy on κ-(BEDT-TTF)$_2$Cu[N(CN)$_2$]Br using STM. *Synthetic Metals* **133-134**, 213-214, (2003).

8 Ugawa, A. & Tanner, D. B. Pseudo gap and superconducting gap in an organic superconductor κ-(BEDT-TTF)$_2$[Cu(SCN)$_2$]. *Physica C: Superconductivity* **341-348**, 2201-2204, (2000).

9 Kindt, J. T. & Schmuttenmaer, C. A. Theory for determination of the low-frequency time-dependent response function in liquids using time-resolved terahertz pulse spectroscopy. *The Journal of Chemical Physics* **110**, 8589-8596, (1999).

10 McGuire, J. J. *et al.* Incoherent interplane conductivity of κ−(BEDT−TTF)$_2$Cu[N(CN)$_2$]Br. *Physical Review B* **64**, 094503, (2001).

11 Kaiser, S. *et al.* Optically induced coherent transport far above T$_c$ in underdoped YBa$_2$Cu$_3$O$_{6+\delta}$. *Physical Review B* **89**, 184516, (2014).

12 Mitrano, M. *et al.* Possible light-induced superconductivity in K$_3$C$_{60}$ at high temperature. *Nature* **530**, 461-464, (2016).

13 Cantaluppi, A. *et al.* Pressure tuning of light-induced superconductivity in K$_3$C$_{60}$. *Nature Physics* **14**, 837-841, (2018).

14 Zimmermann, W., Brandt, E. H., Bauer, M., Seider, E. & Genzel, L. Optical conductivity of BCS superconductors with arbitrary purity. *Physica C: Superconductivity* **183**, 99-104, (1991).

15 Dressel, M. & Grüner, G. *Electrodynamics of Solids*. (Cambridge University Press, 2002).

16 Giannozzi, P. *et al.* Advanced capabilities for materials modelling with Quantum ESPRESSO. *Journal of Physics: Condensed Matter* **29**, 465901, (2017).

17 Giannozzi, P. *et al.* QUANTUM ESPRESSO: a modular and open-source software project for quantum simulations of materials. *Journal of Physics: Condensed Matter* **21**, 395502, (2009).

18 Geiser, U., Kini, A. M., Wang, H. H., Beno, M. A. & Williams, J. M. Structure at 20 K of the organic superconductor [kappa]-di[3,4;3',4'-bis(ethylenedithio)-2,2',5,5'-tetrathiafulvalenium] bromo(dicyanamido)cuprate(I), κ-(BEDT-TTF)$_2$Cu[N(CN)$_2$]Br. *Acta Crystallographica Section C* **47**, 190-192, (1991).

19 Kini, A. M. *et al.* A new ambient-pressure organic superconductor, κ-(ET)$_2$Cu[N(CN)$_2$]Br, with the highest transition temperature yet observed (inductive onset T_C = 11.6 K, resistive onset = 12.5 K). *Inorganic Chemistry* **29**, 2555-2557, (1990).

20 Maksimuk, M., Yakushi, K., Taniguchi, H., Kanoda, K. & Kawamoto, A. The C=C Stretching Vibrations of κ-(BEDT–TTF)$_2$Cu[N(CN)$_2$]Br and Its Isotope Analogues. *Journal of the Physical Society of Japan* **70**, 3728-3738, (2001).

21 Kandpal, H. C., Opahle, I., Zhang, Y.-Z., Jeschke, H. O. & Valentí, R. Revision of Model Parameters for κ-Type Charge Transfer Salts: An Ab Initio Study. *Physical Review Letters* **103**, 067004, (2009).

22 Andrade, X. *et al.* Real-space grids and the Octopus code as tools for the development of new simulation approaches for electronic systems. *Physical Chemistry Chemical Physics* **17**, 31371-31396, (2015).

23 Castro, A. *et al.* octopus: a tool for the application of time-dependent density functional theory. *physica status solidi (b)* **243**, 2465-2488, (2006).

24 Komatsu, T., Matsukawa, N., Inoue, T. & Saito, G. Realization of Superconductivity at Ambient Pressure by Band-Filling Control in κ-(BEDT-TTF)$_2$Cu$_2$(CN)$_3$. *Journal of the Physical Society of Japan* **65**, 1340-1354, (1996).

25 Jeschke, H. O., Kandpal, H. C., Opahle, I., Zhang, Y.-Z. & Valentí, R. First principles determination of the model parameters in κ-(ET)$_2$Cu$_2$(CN)$_3$. *Physica B: Condensed Matter* **405**, S224-S228, (2010).

26 Al-Assam, S., Clark, S. R. & Jaksch, D. The tensor network theory library. *Journal of Statistical Mechanics: Theory and Experiment* **2017**, 093102, (2017).

27 White, S. R. Density matrix formulation for quantum renormalization groups. *Physical Review Letters* **69**, 2863-2866, (1992).

28 Vidal, G. Efficient Classical Simulation of Slightly Entangled Quantum Computations. *Physical Review Letters* **91**, 147902, (2003).